

Reactive power flow optimization in AC drive systems

Sanjay Chandrasekaran^{1,3}, Catalin Arghir¹, Pieder Jörg², Florian Dörfler³ and Silvia Mastellone¹

Abstract— This paper explores a limit avoidance approach in the case of input (modulation) and output (current) constraints with the aim of enhancing system availability of AC drives. Drawing on the observation that, in a certain range of reactive power, there exists a trade-off between current and modulation magnitude, we exploit this freedom and define a constrained optimization problem. We propose two approaches, one in the form of an activation-function which drives the reactive power set-point towards safety, and an approach which uses online feedback optimization to set the reactive power dynamically. Both methods compromise reactive power tracking accuracy for increased system robustness. Through a high fidelity simulation, we compare the benefits of the two methods, highlighting their effectiveness in industrial applications.

I. INTRODUCTION

Medium voltage (MV) drives are widely used in industrial applications, including heat pumps, compressors or wind turbines, where they enable efficient and precise control of large electrical machines at variable speed [1]–[3]. These drives often employ voltage-source converters (VSCs) to regulate power flow and maintain stability and flexibility of operation. However, during some transient events such as overload or grid disturbances, the drive system can experience overcurrent and overmodulation, leading to degraded performance, and in extreme cases, system shutdown. In applications such as oil and gas, the unplanned interruption of the process results in high financial loss, thus system availability requirements are sometimes prioritized over performance and efficiency.

Reactive power in drive systems is typically regulated to zero [4] in order to minimize losses. However, in megawatt-scale applications, MV drives significantly influence grid behavior, making reactive power management a crucial factor [5]. The design of AC drive systems generally involves a tradeoff between efficiency and robustness to grid conditions, allowing some margin for reactive power needed for Static Synchronous Compensator (STATCOM) features [6]. In applications such as wind energy, VSCs actively regulate the point of common coupling (PCC) voltage or may participate to grid forming [7]. In other cases, they provide

This work was supported by the Swiss National Science Foundation under NCCR Automation, grant agreement 51NF40_180545

¹Sanjay Chandrasekaran, Catalin Arghir and Silvia Mastellone are with the Institute of Electric Power Systems, University of Applied Sciences Northwest Switzerland, Windisch, Switzerland.
sanjay.chandrasekaran@fhnw.ch,
catalin.arghir@fhnw.ch, silvia.mastellone@fhnw.ch

²Pieder Jörg is with ABB Motion, ABB Switzerland Ltd., Turgi, Switzerland. pieder.joerg@ch.abb.com

³Sanjay Chandrasekaran and Florian Dorfler are with the Automatic Control Lab (IfA) at ETH Zurich, Switzerland. schandraseka@ethz.ch, dorfler@ethz.ch

ancillary services by allowing the reactive power set-point to be determined by the grid operator or by implementing a droop between reactive power and voltage.

However, the VSC has a limited range of supplying reactive power. Its constraints arise in the static case, due to design limitations, and the dynamic case, as a function of instantaneous active power, DC-link voltage, and grid conditions [8, 9]. We propose a constraint-aware dynamic adaptation of the reactive power set-point that accounts for external demands while respecting system constraints.

In this study, we investigate two competing methods, an activation-function approach and an optimization-based technique leveraging Online Feedback Optimization (OFO). Both methods operate as outer-loops to existing controllers with anti-windup limiters, preventing them from entering the saturated mode of operation whenever possible. By integrating these strategies, we enhance both transient and steady-state performance when compared to state-of-the art current limiters [10]–[12].

In the context of power systems, various types of strategies for limiting converter current are employed [13]–[16]. We aim to leverage the relationship between anti-windup and the projected gradient descent mechanism found in OFO [17]. In a similar scenario [18], OFO is used to steer fast nonlinear dynamics. In [19], it is used to optimize reactive power flow in a distribution grid by prescribing the inverter set-points while enforcing voltage constraints. In our work, we take a deeper look into the single-inverter case and enforce constraints with the aim of internal stability.

The rest of the paper is organized as follows: Section II formulates the problem, describing the system model, control assumptions, and constraints. Section III goes over the control design, while Section IV presents the OFO convergence guarantees. Section V provides simulation results that illustrate the performance improvements achieved by the proposed methods. Finally, Section VI concludes the paper with a discussion of key findings.

II. PROBLEM STATEMENT

We consider a power conversion system consisting of a grid-side converter, a DC-link capacitor, a motor-side converter, an electrical machine, and a driveline shaft attached to a motoring or generating load. The main role of the grid-side converter, is to deliver active power by regulating the DC-link voltage, and thus allow the motor-side converter to supply the load under a wide range of external conditions.

Our main goal is to design an outer loop for the reactive-power component of the grid current reference in order to

avoid overmodulation or overcurrent limits and preserve DC-link regulation. Our proposal is to exploit a trade-off between converter current and modulation constraints and override the external reactive power set-point.

Assumption 1: The drive system is modelled based on the following set of assumptions:

- i. The drive system is designed such that, during grid voltage or load transients, the grid-side current limit may be reached;
- ii. Changes in set-points, load torque, and the grid voltage have limited bandwidth;
- iii. We assume a balanced grid and omit the regulation of the zero-sequence current and of the mid-point voltage from our analysis;
- iv. The inner loop of the motor-side converter is assumed to have sufficiently fast bandwidth such that, together with the motor dynamics, it can be abstracted out of the overall model by assuming that the motor torque is perfectly tracking its set-point.

A. Drive system model

In the rest of this section, we explain a typical industrial drive and its core control system. We propose to use the following energy-preserving, average-switch model of a back-to-back drive system

$$M\dot{w} = -Dw + \tau_m - \tau_l \quad (1a)$$

$$C_{dc}\dot{v}_{dc} = -G_{dc}v_{dc} - \frac{w}{v_{dc}}\tau_m + m_g^\top i_g \quad (1b)$$

$$L_g\dot{i}_g = -Z_g i_g + v_g - m_g v_{dc}, \quad (1c)$$

where M, D are the moment of inertia and viscous damping of the driveshaft, w its angular velocity, τ_m is the motor air-gap torque (control input), τ_l is the driveshaft load torque (unmeasured disturbance), v_{dc} is the DC-link voltage, C_{dc} its capacitance and G_{dc} its parallel conductance. Furthermore, $m_g \in \mathbb{R}^2$ is the grid-side converter dq -modulation vector (control input), $L_g, R_g > 0$ phase inductance and resistance, respectively, $i_g \in \mathbb{R}^2$ is the grid current (towards the converter) and $v_g \in \mathbb{R}^2$ is the voltage in dq -coordinates (measured disturbance). Finally, the grid impedance is defined as

$$Z_g = \begin{bmatrix} R_g & -\omega_0 L_g \\ \omega_0 L_g & R_g \end{bmatrix}. \quad (2)$$

We use the well established notions of instantaneous power [20] and the power-invariant dq -frame transformation as

$$x_{abc} \mapsto x_{dq0} = T_{\theta_g} T_{\alpha\beta\gamma} x_{abc}, \quad (3)$$

such that $T_{\alpha\beta\gamma}^{-1} = T_{\alpha\beta\gamma}^\top$ and $T_{\theta_g}^{-1} = T_{\theta_g}^\top$, and assume that the grid voltage angle θ_g is measured. Moreover, by virtue of the third-harmonic injection, the maximum modulation amplitude in dq -coordinates becomes $\frac{1}{\sqrt{2}}$.

Remark 1: In this model, we omit the motor and its torque control dynamics, an abstraction which enables us to focus on the outer-loop behavior. Our motivation is based on the fact that most modern MV motor controllers adopt a form of direct Model predictive control (MPC), or Direct torque control (DTC) [21, 22], to track the torque set-point with high bandwidth [23].

B. Drive system objectives

We consider the following tracking objectives,

$$w \rightarrow w^{\text{ref}} \quad (4)$$

$$v_{dc} \rightarrow v_{dc}^{\text{ref}} \quad (5)$$

$$Q_g = v_g^\top J i_g \rightarrow Q_g^*, \text{ where } J = \begin{bmatrix} 0 & -1 \\ 1 & 0 \end{bmatrix}, \quad (6)$$

while rejecting external disturbance τ_l, v_g . Moreover, $|w^*| \leq w_{\max}$ and $|Q_g^*| \leq Q_{\max}$ are slowly changing external set-points. The system is subject to fast changing loads $|\tau_l| \leq \tau_{\max}$ and occasional dips in $\|v_g\| \leq v_{g,\max} = \alpha_v v_{g,\text{nom}}$ with e.g. $\alpha_v = 1.1$ representing a grid code overvoltage limit. We also consider some margin for producing reactive power

$$\tau_{\max} w_{\max} = P_{g,\max} = \frac{1}{\alpha_q} \sqrt{P_{g,\max}^2 + Q_{g,\max}^2}, \quad (7)$$

where e.g. $\alpha_q = 1.2$ is a de-rating factor, such that the maximum current amplitude becomes $i_{g,\max} = \frac{\alpha_q P_{g,\max}}{v_{g,\text{nom}}}$.

C. Inner loop definition

The standard practice involves a cascade of PI controllers with anti-windup. We consider the speed control as

$$\dot{x}_m \simeq w - w^{\text{ref}} \quad (8a)$$

$$\tau_m = \underset{|\cdot| \leq \tau_{\max}}{\text{sat}} (-K_{p,m}(w - w^*) - K_{i,m}x_m), \quad (8b)$$

where $K_{p,m} = 2\zeta_m \omega_m M$, and $K_{i,m} = \omega_m^2 M$, with tunable ω_m and ζ_m , and sat represents the result of bounding the argument in absolute value (or in norm for the multivariable case). We use \simeq to symbolize the presence of anti-windup control. The DC-link control is defined as

$$\dot{x}_{dc} \simeq v_{dc} - v_{dc}^{\text{ref}} \quad (9a)$$

$$P_g^* = \underset{|\cdot| \leq P_{g,\max}}{\text{sat}} (-K_{p,dc}(v_{dc} - v_{dc}^{\text{ref}}) - K_{i,dc}x_{dc})v_{dc}^{\text{ref}} + \tau_m w^*, \quad (9b)$$

where $K_{p,dc} = 2\zeta_{dc} \omega_{dc} C_{dc}$, and $K_{i,dc} = \omega_{dc}^2 C_{dc}$, with tunable ω_{dc} and ζ_{dc} . Moreover, the reference for the motor torque is used as feed-forward from the speed controller. For the grid-side current reference we consider a circular current limiter, as described in Fig. 2 and below

$$i_g^* = \underset{|\cdot| \leq i_{g,\max}}{\text{sat}} \frac{1}{\|v_g\|^2} \begin{bmatrix} v_g^\top \\ v_g^\top J \end{bmatrix} \begin{bmatrix} P_g^* \\ Q_g^* \end{bmatrix}. \quad (10)$$

Finally, the current controller also adopts a feedforward

$$\dot{x}_g \simeq i_g - i_g^* \quad (11a)$$

$$m_g = \underset{\|\cdot\| \leq \frac{1}{\sqrt{2}}}{\text{sat}} \frac{1}{v_{dc}^{\text{ref}}} (v_g - Z_g i_g^* + K_{p,g}(i_g - i_g^*) + K_{i,g}x_g), \quad (11b)$$

where $K_{p,g} = 2\zeta_g \omega_g L_g$, and $K_{i,g} = \omega_g^2 L_g$, with tunable ω_g and ζ_g . In this scenario we take $\zeta_m, \zeta_{dc}, \zeta_g = 1$, and set both ω_{dc}, ω_m much smaller than current control bandwidth ω_g , enforcing the typical time-scale separation.

III. CONTROL PROBLEM

We are now ready to state our main control problem.

Problem 1: Consider the system (1) in feedback with (8)-(11). Prescribe a feedback law on Q_g^* such that the limits corresponding to the constraints $\|i_g\| \leq i_{g,\max}$ and $\|m_g\| \leq \frac{1}{\sqrt{2}}$ are avoided at trade-off with an external set-point.

Our intuition is based on the fact that when Q_g^* is set to zero, the current magnitude (and therefore power losses) are minimized, and when Q_g^* is set to

$$Q_g^{mm} = \frac{\omega_0 L_g \|v_g\|^2}{\|Z_g\|^2}, \quad (12)$$

the modulation amplitude is minimized, and therefore robustness is improved. The latter is seen by inserting (10) into (11b) and taking the norm

$$\|m_g\|^2 v_{dc}^{ref2} = \|v_g\|^2 - 2R_g P_g^* - 2\omega_g L_g Q_g^* + \frac{\|Z_g\|^2}{\|v_g\|^2} (P_g^{*2} + Q_g^{*2}),$$

and noticing that the gradient is zero at Q_g^{mm} ,

$$\nabla_{Q_g^*} \|m_g\|^2 = \frac{2}{v_{dc}^{ref2}} (-\omega_g L_g + \frac{\|Z_g\|^2}{\|v_g\|^2} Q_g^*). \quad (13)$$

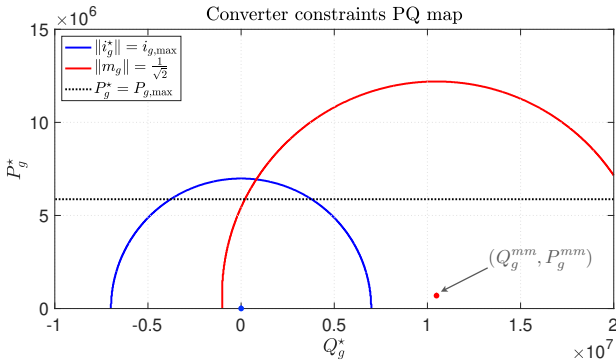


Fig. 1. The PQ diagram for the considered drive system (motoring) at nominal DC-link and grid voltage levels, where the admissible Q_g set-point is determined mainly by the active power demand.

As seen in Fig. 1, for our converter design, the trade-off between current and modulation magnitude is present in most of the admissible range of operation. Note that it is easier for the VSC to inject positive rather than negative (or capacitive) reactive power into the grid, and, in order for the drive system to act as a STATCOM, a sufficient DC-bus margin must be provided.

A. Activation-function approach

Our first proposal is to use a low-pass filter on the external reference which is deterred to safety values when the corresponding limits are reached

$$\dot{Q}_g^* = -\omega_q (Q_g^* - Q_g^{ref}) - \kappa_1 \Gamma_1(i_g^*) Q_g^* - \kappa_2 \Gamma_2(m_g) (Q_g^* - Q_g^{mm}). \quad (14)$$

Here $\omega_q > 0$ is the speed at which tracks the unconstrained set-point Q_g^{ref} . Furthermore, $\kappa_1, \kappa_2 > 0$ are gains on the

sensitivity to constraint violations for i_g^* , respectively m_g , and the two positive functions

$$\Gamma_1(i_g^*) = \|i_g^*\| - \min(\|i_g^*\|, i_{g,\max}) \quad (15)$$

$$\Gamma_2(m_g) = \|m_g\| - \min(\|m_g\|, \frac{1}{\sqrt{2}}), \quad (16)$$

are activations of the gradients that drive Q_g^* to the values that mitigate the corresponding constraint violations.

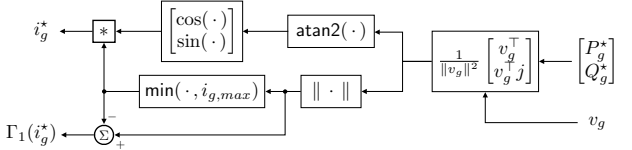


Fig. 2. Block diagram of the circular current reference limiter together with the barrier activation Γ_1 .

Note that, in Fig. 3, the integrator saturation block implements, for simplicity, a rectangular limiter on each dq -component circumscribing the circular limit $\|m_g\| \leq \frac{1}{\sqrt{2}}$. The role of Γ_2 is to keep the modulation magnitude bounded by indirectly driving the integrator away from saturation.

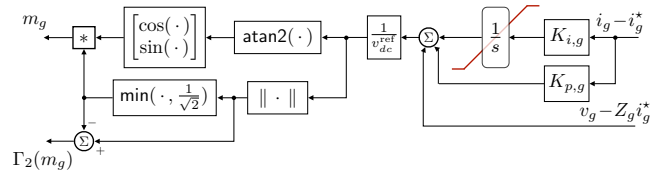


Fig. 3. Block diagram of the circular modulation limiter together with the barrier activation Γ_2 .

Remark 2: It is important to assign higher priority to the modulation constraint by tuning $\kappa_1 \ll \kappa_2$, as the converter loses its ability to track i_g^* and therefore is unable to limit the current when the modulation constraint limit is reached.

Remark 3: An alternative to the circular limiter may be one with active-power priority [24]. However, our approach has the advantage of being sensitive, in addition, to the (asymmetric) saturation of the modulation magnitude.

Despite its simplicity and compatibility with existing saturation mechanisms, this method lacks formal convergence guarantees, which leads to our next proposal.

B. OFO: Problem Formulation

An alternative view to preserving the drive system operation is to iteratively compute a suitable set point Q_g^* satisfying current and modulation constraints. Thus, a steady-state optimization algorithm such as OFO [25, Section 3] is naturally convenient. We define a real-time optimization problem as

$$\underset{Q_g^*}{\text{minimize}} \quad \varphi(Q_g^*, i_g^*) \quad (17a)$$

$$\text{s.t.} \quad i_g^* = h(Q_g^*, d) \quad (17b)$$

$$Q_g^* \in \mathcal{C}, \quad (17c)$$

where, $\varphi(i_g, Q_g^*) = \frac{1}{2}(\|i_g\|^2 + \gamma\|Q_g^* - Q_g^{\text{ref}}\|^2)$, with γ being a non-negative trade-off parameter between minimizing the current i_g and the deviation of the reactive power set-point Q_g^* from its external reference Q_g^{ref} . Since the natural choice for current minimization is minimizing Q_g^* , we construct a composite cost function including the term $\|Q_g^* - Q_g^{\text{ref}}\|^2$ as a soft constraint that restricts Q_g^* from deviating significantly from an external reference Q_g^{ref} . The steady-state map $i_g^* = h(Q_g^*, d(k))$ is described in (10) where $d(k) = (P_g^*(k), v_g(k))$ represents a time-varying disturbance vector. The constraints $\mathcal{C}(k)$ represent limits on the current and modulation amplitude at timestep k . Using (10) and (11b), the current constraint $\|i_g^*\|^2 \leq i_{g,\max}^2$ and modulation constraint $\|m_g\|^2 \leq \frac{1}{2}$ at each operating point are written in terms of Q_g^* as follows, respectively:

$$\begin{aligned} \mathcal{C}(k) = & \left\{ Q_g^* : P_g^{*2}(k) + Q_g^{*2} \leq \|v_g(k)\|^2 i_{g,\max}^2, \right. \\ & \left. \|v_g(k) - Z_g h(Q_g^*, d(k))\|^2 \leq \frac{1}{2} (v_{dc}^{\text{ref}})^2 \right\} \end{aligned} \quad (18)$$

Remark 4: Since the cost function $\varphi(Q_g^*, i_g)$ is strongly convex in Q_g^* and steady-state map $h(Q_g^*, d(k))$ affine with respect to Q_g^* and $\mathcal{C}(k)$ convex at every time instant k , the resulting optimization problem in (17) is strongly convex and admits a unique solution trajectory $\{i_g^*(k), Q_g^*(k)\}_{k=0}^N$ for every unique load disturbance sequence $\{d(k)\}_{k=0}^N$.

C. OFO: Problem Solution

Using OFO, we approach Problem 1 with a feedback controller based on the following projected gradient descent algorithm [17, Section II.D]:

$$Q_g^*(k+1) = \Pi_{\mathcal{C}(k)}[Q_g^*(k) - \mu(k)\zeta(k)\Phi(Q_g^*(k), i_g(k+1))], \quad (19)$$

where μ is the learning rate, $\Pi_{\mathcal{C}(k)}[\cdot]$ is the Euclidean projection onto set $\mathcal{C}(k)$, and the composite gradient

$$\Phi(Q_g^*, i_g) = \nabla_{Q_g^*}\varphi(Q_g^*, i_g) + \nabla_{Q_g^*}h(Q_g^*, d(k))^T \nabla_{i_g}\varphi(Q_g^*, i_g)$$

results from the chain-rule of differentiating the cost $\varphi(Q_g^*, h(Q_g^*, d(k)))$. As in every OFO algorithm, we replace the steady-state value of i_g in (10) with its real-time measurement $i_g(k+1)$ assuming that i_g has reached a local steady-state [19]. In practice, this time-scale separation between the system and the controller can be enforced by introducing a periodic trigger [26, Section III.B] that produces a new OFO solution every m time steps (i.e. $\zeta(k) = 1$ if $k = lm$, where $l = \{0, 1, 2, \dots\}$ and $\zeta(k) = 0$ if $k \neq lm$). Thus, the sampling time of the OFO and the system are related with $T_s = mT_c$, with T_s being the sampling time of the OFO and T_c that of the system.

IV. CONVERGENCE GUARANTEES

Here, we provide convergence guarantees for the closed-loop system, with the inner-loop (1a)-(1c) regulated using the PI controllers (8a),(9a),(11a) and the outer-loop controlled by

the OFO based on the projected gradient descent algorithm in (19). We make the following assumption regarding the inner-loop and the disturbances, respectively:

Assumption 2: The PI controllers (8a),(9a),(11a) are tuned such that the inner-loop is locally exponentially stable for a constant input Q_g^* and disturbance d , i.e. $\exists C_1, C_2 : \|i_g(k) - h(Q_g^*, d)\| \leq C_1\|i_g(0) - h(Q_g^*, d)\|e^{-C_2 k}$

Assumption 3: The disturbance $d(k)$ is piece-wise constant with respect to the sampling rate of OFO, i.e. $d(lm) = d(lm+1) = \dots = d(lm+m-1), \forall l \in \{0, 1, 2, \dots\}$.

Assumption 3 quantitatively describes bandwidth limitations on the disturbances and load (see Assumption 1(ii)).

To analyze convergence guarantees, we use the metric $\psi(k) = |Q_g^*(k) - \bar{Q}_g^*(k)|$ that describes the distance of the OFO solution from its global optimum $\bar{Q}_g^*(k)$ at time k .

Theorem 1: Let Assumptions 1,2, 3 hold. For any learning rate $\mu(k) \in (0, \frac{2\|v_g(k)\|^2}{1+\gamma\|v_g(k)\|^2})$, the sequence of $Q_g^*(k)$ generated using (19) satisfies the following recursive relation:

$$\begin{aligned} \psi((l+1)m) \leq & \epsilon(lm)\psi(lm) + \underbrace{|\Delta\bar{Q}_g^*(lm)|}_{\mathcal{T}_1} + \\ & \underbrace{C_1 C_3 \|v_g(lm)\| \|i_g(lm) - i_g^*(lm)\| e^{-C_2}}_{\mathcal{T}_2}, \end{aligned} \quad (20)$$

where, $\Delta\bar{Q}_g^*(k) = \bar{Q}_g^*(k) - \bar{Q}_g^*(k+1)$, $\epsilon(k) = 1 - \mu(k)(\gamma + \|v_g(k)\|^2)$, $i_g^*(k) = h(Q_g^*(k), d(k))$, the constants C_1, C_2 resulting from Assumption 2 and C_3 from using $\mu(k) = C_3\|v_g(k)\|^2$, $C_3 \in (0, 2/(1 + \gamma v_{g,\max}^2))$.

Proof: Refer to Appendix VII-A ■

The above theorem shows that with an appropriate choice of $\mu(\cdot)$ such that $|\epsilon(\cdot)| < 1$, the distance of the OFO trajectory from its optimal solution is contracting, with the offset terms \mathcal{T}_1 accounting for the difference in the optimal reactive power between two trigger time instances and \mathcal{T}_2 accounting for the disturbance $v_g(\cdot)$ and the distance of $i_g(\cdot)$ from the new steady-state point $i_g^*(\cdot)$.

Corollary 1: As $l \rightarrow \infty$, the distance of the OFO solution from its optimal trajectory is given by:

$$\lim_{l \rightarrow \infty} \psi(lm) \leq \frac{1}{1 - \epsilon_{\max}} \left(|\Delta\bar{Q}_g^*(m)| + \frac{2C_1 C_3 \alpha_q P_{g,\max} e^{-C_2 m}}{1 - C_1 e^{-C_2 m}} \right), \quad (21)$$

where, $|\Delta\bar{Q}_g^*(m)| = \max_k |\Delta\bar{Q}_g^*(k)|$, $\epsilon_{\max} = \max_k |\epsilon(k)|$ with $\epsilon_{\max} < 1$, α_q de-rating factor (see (7)) and $P_{g,\max}$ maximum active power.

Proof: Refer to Appendix VII-A ■

From the above Corollary, it can be observed that asymptotic convergence of the OFO solution to the optimal trajectory of (17) is limited by the absolute maximum change in optimal reactive power between two OFO sampling times and the absolute maximum active power. Since $m = T_s/T_c$, we observe that convergence depends on the OFO sampling period T_s . A large T_s promotes more time-scale separation between the inner-loop and the OFO controller, leading to the OFO trajectory being in close proximity to the optimal

solution. However, a trade-off must be established, as an exceedingly large T_s renders Assumption 3 impractical.

V. EXPERIMENTAL RESULTS

We simulate an MV drive system consisting of a 7MVA converter with grid-side transformer and a 5kV DC-bus with mid-point. The converter is implemented using an average-model of the three-level neutral-point-clamped (NPC) topology. On the load-side, we implement a switching-model of the three-level NPC converter connected to an Induction Machine (IM) model whose rotor is part of a 6MW driveline shaft modelled as a 5-mass torsional system. The air-gap torque τ_m acts on one end of the shaft and the load τ_l on the other. The motor torque is produced through (an industry-standard) direct Model Predictive Control (MPC) which takes τ_m as reference. As illustrated in Fig. 4, the control structure described in Section II-B is in place.

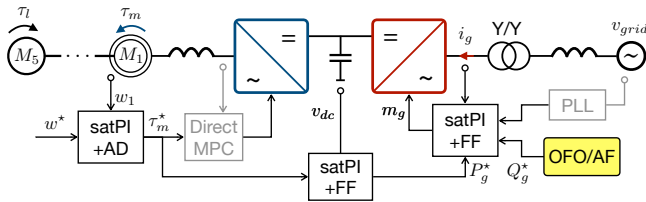


Fig. 4. Block diagram of the simulated setup. From left to right: speed control, torque control, voltage control and current control loops typically implemented in a drive system, together with a Phase-locked-loop (PLL) that extracts the grid voltage and the angle for the dq -transformation (as seen on the converter side of the transformer). The anti-windup tracking controllers are denoted by satPI, while further feed-forward (FF) and active-damping (AD) terms are appropriately added to improve the fidelity of the simulation.

All controllers, except for the OFO, were implemented with a sample time of $T_c = 250\mu s$ while the plant dynamics were discretized with a sampling time of $25\mu s$. The two reactive power controllers were tuned as follows

- Activation-function: $\omega_q = 2\pi 5$, $\kappa_1 = 0.1$, $\kappa_2 = 250$, with soft-max Γ_1 at $i_{g,\max}$ and soft-max Γ_2 at $\frac{0.97}{\sqrt{2}}$;
- OFO: $k_\mu = 80$, $k_\gamma = 4$, $T_s = 10^{-3}s$, where

$$\mu = k_\mu T_s \|v_g\|^2, \quad \gamma = \frac{k_\gamma T_s}{\|v_g\|^2}, \quad (22)$$

with modulation limit set to $\frac{0.93}{\sqrt{2}}$.

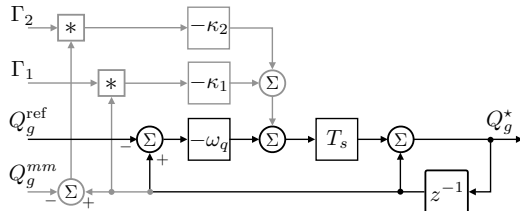


Fig. 5. Block diagram of the Forward Euler implementation of the activation function controller (14).

We perform three tests in which we compare the response of three scenarios: using (a) OFO, (b) Activation-function-based approach and (c) unmitigated, i.e. $Q_g^* = Q_g^{\text{ref}}$.

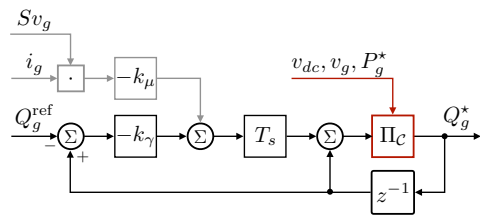


Fig. 6. Block diagram of the OFO algorithm implementation, where $S = \begin{bmatrix} 0 & 1 \\ 1 & 0 \end{bmatrix}$ is part of the sensitivity function Φ , with (22) entering into (19).

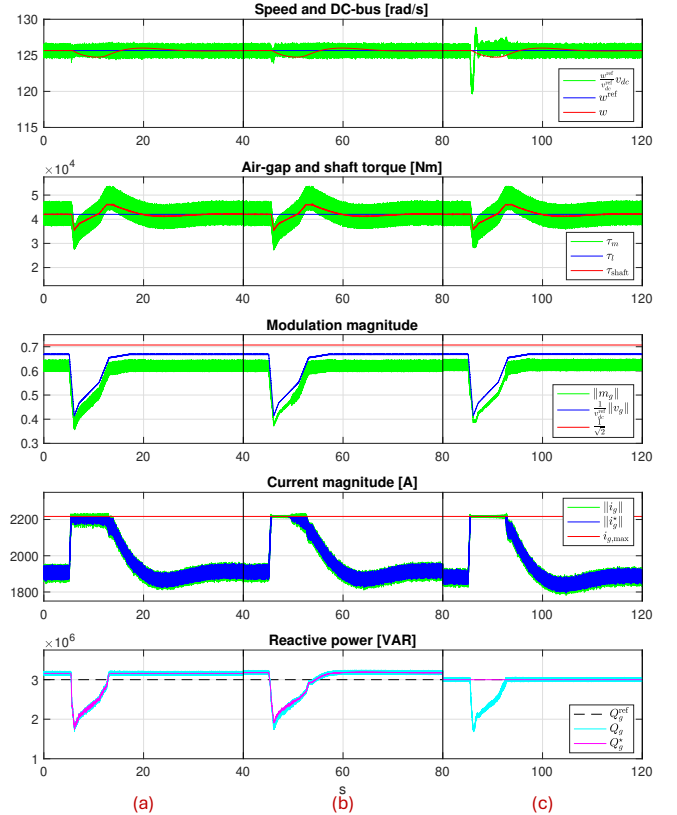


Fig. 7. Plots of the three responses to the a profile: (a) OFO approach, (b) Activation-function approach, and (c) $Q_g^* = Q_g^{\text{ref}}$. In the first plot we see the rigid-body shaft speed w in red, its reference in blue, and the DC-link voltage (scaled to units of speed) in green. In the second plot we see the air-gap torque τ_m in green, the load torque τ_l in blue, and a mid-shaft torque τ_{shaft} in red. In the third plot we see the modulation amplitude $\|m_g\|$ in green compared to the magnitude of the grid voltage scaled by the DC-bus in blue, and the limit of the modulation amplitude in red. In the fourth plot we see the current magnitude in green, the reference magnitude in blue and its limit in red. In the last plot we see the reactive power in cyan, its external reference in black, and the dynamic set-point in purple.

A. Voltage dip

We set the reference speed to w_{\max} and the load to $0.9\tau_{\max}$, amounting to about 5.3 MW of motoring power, and we set the reactive power demand to 3 MVAR. We subject the drive system to a 40% gradual dip in the amplitude of the grid voltage. Fig. 7 shows the reactive power drop during transient, either driven by the set-point adaptation in cases (a) and (b), or induced by the balanced saturation of current reference magnitude in case (c). This test shows how the

two proposed techniques produce an effect on reactive power and current magnitude similar to that of the circular current limiter but with direct intervention on the Q_g^* set-point rather than as a consequence of the saturation of i_g^* .

B. Reference step

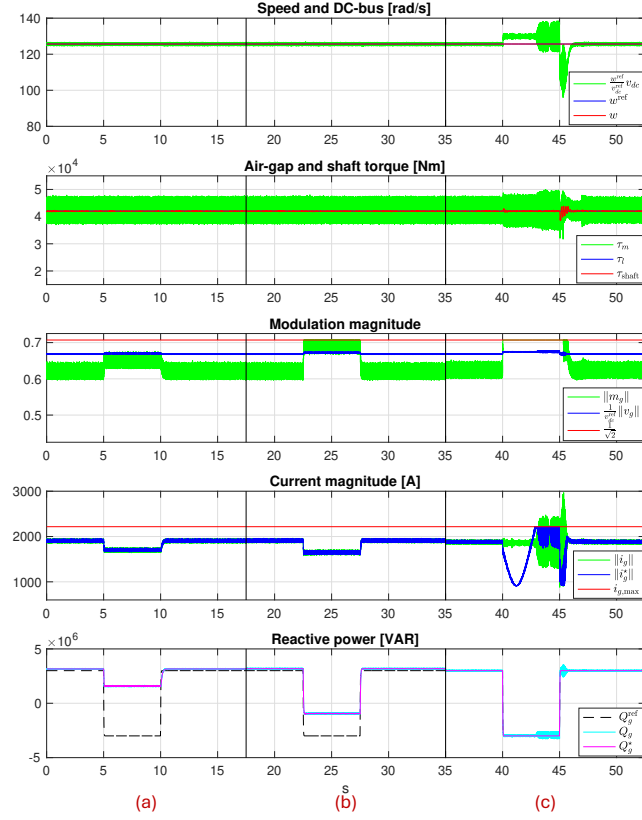


Fig. 8. Plots of the three responses to a reactive power demand outside of the constraint set: (a) OFO approach, (b) Activation-function approach, and (c) $Q_g^* = Q_g^{\text{ref}}$. Traces are as described in Fig. 7.

We apply a 5 second set-point change from 3 MVAR to (an infeasible) -3 MVAR, and back to 3 MVAR at the same load conditions as before. In Fig. 8, we see how the two proposed methods (a) and (b) arrive at different trade-off between tracking the external reactive-power set-point and satisfying the modulation magnitude constraint. In the unmitigated case (c), we see how the current controller is no longer able to track the reference and goes into overcurrent (even though its reference is limited) as a consequence of modulation saturation. In addition, the DC-bus voltage loses regulation, reaches tripping levels, and disrupts motor-side operation.

C. Overvoltage

In our third test, we leave the speed reference at w_{\max} and set the load torque to $-0.8\tau_{\max}$. In this generator scenario, the reactive power reference is set to zero, and the grid undergoes a 12% overvoltage for 5 seconds. We see in Fig. 9 that the proposed methods (a) and (b) produce slightly higher reactive power at steady-state, but ride through the

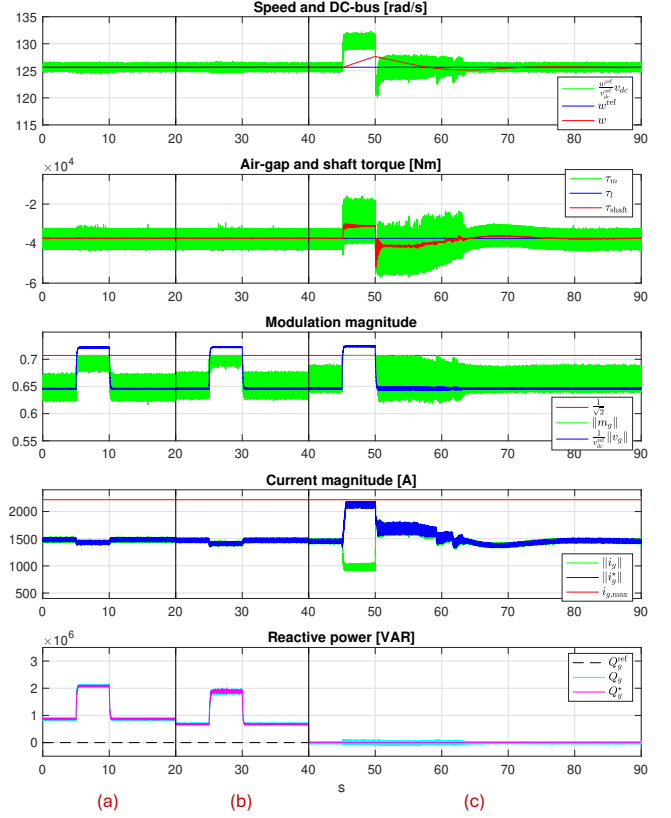


Fig. 9. Plots of the three responses to a severe grid overvoltage: (a) OFO approach, (b) Activation-function approach, and (c) $Q_g^* = Q_g^{\text{ref}}$. Traces are as described in Fig. 7.

overvoltage. In the unmitigated case (c), the modulation saturates and produces an uncontrolled condition where a significant energy imbalance between motor-side and grid-side occurs. In this scenario, the (circular) current limiter is not in effect; in fact, not enough current is produced, and the motor-side energy is trapped in the driveshaft mass, causing it to overspeed. In addition, the DC-bus is overcharged and reaches tripping levels.

VI. CONCLUSION

This paper presents a novel approach to constraint-aware reactive power control in AC drives by leveraging the trade-off between input (modulation) and output (current) constraints. We draw the contrast between an activation-function method and an online feedback optimization approach. The proposed techniques are meant to complement the saturation mechanisms which are already in place, in order to improve the performance and extend the availability of the drive system by compromising reactive power tracking error. Our detailed simulation highlights the similarity of the two methods in mitigating system-wide fault conditions, showcasing their advantage over a conventional current limiter. That is, by maintaining the reactive power within the limits induced by the grid and load conditions, our approach avoids the saturation of the modulation vector, which in turn preserves the current tracking and the DC-bus regulation capability of

the grid-side converter, to the extent possible. As a result, the operation of the drive system is enhanced with minimum conservatism.

VII. APPENDIX

A. Proof of Theorem 1

We consider $\psi(k) = |Q_g^*(k) - \bar{Q}_g^*(k)|$, the distance between the OFO solution and the optimal trajectory as a performance criterion to show convergence guarantees as the problem (17) is strongly convex (see Remark 4).

Note that in the time instants where the OFO is not triggered, we have $Q_g^*(k+1) = Q_g^*(k)$. Further, since the disturbance is piece-wise continuous with respect to the OFO sampling rate (see Assumption 3), the optimal trajectory $\bar{Q}_g^*(k)$ remains constant between two OFO sampling times. Thus, the following relation can be obtained when the OFO is not triggered (i.e. $\zeta(k) = 0$):

$$\psi(k+1) \leq \psi(k). \quad (23)$$

In the case where the OFO is triggered at time k (i.e. $\zeta(k) = 1$), we have the following inequality:

$$\psi(k+1) \leq |Q_g^*(k+1) - \bar{Q}_g^*(k)| + |\Delta\bar{Q}_g^*(k)|, \quad (24)$$

where, $\Delta\bar{Q}_g^*(k) = \bar{Q}_g^*(k) - \bar{Q}_g^*(k+1)$ is the change in the optimal reactive power between two OFO trigger time instances. Note that the optimal reactive power satisfies the stationarity condition $\bar{Q}_g^*(k) = \Pi_{\mathcal{Q}}[Q_g^*(k) - \mu(k)\Phi(\bar{Q}_g^*(k), \bar{i}_g^*(k))]$, where $\bar{i}_g^*(k) = h(\bar{Q}_g^*(k), d(k))$ and $\Phi(Q_g, i_g)$ is the composite gradient, as defined in (19). We now use the projected gradient descent update on $Q_g^*(k+1)$ and stationarity condition on $\bar{Q}_g^*(k)$ in (23). We also use the fact that projection over a convex set is contractive (i.e. $\|\Pi_{\mathcal{C}}[x] - \Pi_{\mathcal{C}}[y]\| \leq \|x - y\|, \forall x, y \in \mathbb{R}^n$) to obtain

$$\begin{aligned} \psi(k+1) &\leq \left| (1 - \gamma\mu(k))(Q_g^*(k) - \bar{Q}_g^*(k)) - \mu(k)(H(k)^\top i_g(k+1) + \right. \\ &\quad \left. \bar{H}(k)^\top \bar{i}_g^*(k)) \right| + |\Delta\bar{Q}_g^*(k)|, \end{aligned} \quad (25)$$

where, $H(k) = \nabla_{Q_g^*} h(Q_g^*(k), d(k))$ and $\bar{H}(k) = \nabla_{\bar{Q}_g^*} h(\bar{Q}_g^*(k), d(k))$, the sensitivities of the steady-state map $h(Q_g^*, d(k))$ to Q_g^* at $Q_g^*(k)$ and \bar{Q}_g^* , respectively. Since the map $h(Q_g^*, d(k))$ is affine with respect to Q_g^* (17b), $H(k) = \bar{H}(k), \forall k \geq 0$. Thus, (25) can be written as

$$\begin{aligned} \psi(k+1) &\leq \underbrace{\left| (1 - \gamma\mu(k))(Q_g^*(k) - \bar{Q}_g^*(k)) - \mu(k)H(k)^\top(i_g(k) - \bar{i}_g^*(k)) \right|}_{\mathcal{T}_1} + \\ &\quad \underbrace{\left| \mu(k)H(k)^\top(i_g(k+1) - i_g^*(k)) \right| + |\Delta\bar{Q}_g^*(k)|}, \end{aligned} \quad (26)$$

where we add and subtract the term $\mu(k)H(k)^\top i_g^*(k)$ with $i_g^*(k) = h(Q_g^*(k), d(k))$ being the steady-state current at time k . Before we develop inequalities for terms $\mathcal{T}_1, \mathcal{T}_2$, we make the following observation:

Remark 5: The steady-state map $h(Q_g^*, d(k))$ is Lipschitz continuous with respect to Q_g^* with Lipschitz constant $\|v_g(k)\|^{-1}$, i.e. $\|H(k)\| \leq \|v_g(k)\|^{-1} \forall k \geq 0$

We now focus on the term \mathcal{T}_1 :

$$\begin{aligned} \mathcal{T}_1^2 &= (1 - \gamma\mu(k))^2(Q_g^*(k) - \bar{Q}_g^*(k))^2 + \mu(k)^2(H(k)^\top(i_g^*(k) - \bar{i}_g^*(k)))^2 \\ &\quad - 2\mu(k)(1 - \gamma\mu(k))H(k)^\top(i_g^*(k) - \bar{i}_g^*(k))(Q_g^*(k) - \bar{Q}_g^*(k)) \\ &\stackrel{(a)}{\leq} (1 - \gamma\mu(k))^2(Q_g^*(k) - \bar{Q}_g^*(k))^2 + \mu(k)^2\|v_g(k)\|^{-4}(Q_g^*(k) - \bar{Q}_g^*(k))^2 \\ &\quad - 2\mu(k)(1 - \gamma\mu(k))H(k)^\top(i_g^*(k) - \bar{i}_g^*(k))(Q_g^*(k) - \bar{Q}_g^*(k)) \\ &\stackrel{(b)}{\leq} ((1 - \gamma\mu(k))^2 + \mu(k)^2\|v_g(k)\|^{-4})(Q_g^*(k) - \bar{Q}_g^*(k))^2 \\ &\quad - 2\mu(k)(1 - \gamma\mu(k))\|v_g(k)\|^{-2}(Q_g^*(k) - \bar{Q}_g^*(k))^2 \\ &\leq (1 - \gamma\mu(k) - \mu(k)\|v_g(k)\|^{-2})^2\psi(k)^2. \end{aligned} \quad (27)$$

In (a), we make use of norm sub-multiplicativity, i.e. $(H(k)^\top(i_g^*(k) - \bar{i}_g^*(k)))^2 \leq \|H(k)\|^2\|i_g^*(k) - \bar{i}_g^*(k)\|^2$. We then make use of the Lipschitz property on $h(Q_g^*, d(k))$ to state that $\|H(k)\|^2 \leq \|v_g(k)\|^{-2}$ and $\|i_g^*(k) - \bar{i}_g^*(k)\|^2 \leq \|H(k)\|^{-2}(Q_g^*(k) - \bar{Q}_g^*(k))^2$. In (b), we used the explicit analytical form for $H(k), i_g^*(k), \bar{i}_g^*(k)$. Thus, we have the term $\mathcal{T}_1 \leq |\epsilon(k)|\psi(k)$, where $\epsilon(k) = 1 - \mu(k)(\gamma + \|v_g(k)\|^{-2})$. By choosing $\mu(k) \in (0, \frac{2\|v_g(k)\|^2}{1+\gamma\|v_g(k)\|^2})$, we ensure $|\epsilon(k)| < 1, \forall k \geq 0$.

We now focus on the term \mathcal{T}_2 .

$$\begin{aligned} \mathcal{T}_2 &\stackrel{(a)}{\leq} \mu(k)\|v_g(k)\|^{-1}\|i_g(k+1) - i_g^*(k)\| \\ &\stackrel{(b)}{\leq} C_1 C_3 \|v_g(k)\| \|i_g(k) - i_g^*(k)\| e^{-C_2} \end{aligned} \quad (28)$$

In (a), we make use of Lipschitz property on $H(k)$ to state that $H(k) \leq \|v_g(k)\|^{-1}$. In (b), we make use of Assumption 2 to state that $\|i_g(k+1) - i_g^*(k)\| \leq C_1\|i_g(k) - i_g^*(k)\|e^{-C_2}$. Further, we choose $\mu = C_3\|v_g(k)\|^2$ and weight $\gamma(k) = C_4/\|v_g(k)\|^2$ with $C_3 \in (0, 2/(1 + \gamma v_{g,max}^2))$ for feasible guarantees and a more simplified convergence criterion with respect to the learning rate.

Using (27), (28) in (26), we obtain

$$\begin{aligned} \psi(k+1) &\leq |\epsilon(k)|\psi(k) + |\Delta\bar{Q}_g^*(k)| + \\ &\quad C_1 C_3 \|v_g(k)\| \|i_g(k) - i_g^*(k)\| e^{-C_2} \end{aligned}$$

Replacing k with lm in the above and using (23) to state that $\psi((l+1)m) \leq \psi(lm+1)$, we obtain (20). To prove asymptotic convergence, we trace (20) recursively till its initial conditions to obtain:

$$\begin{aligned} \psi(lm) &\leq \epsilon_{max}^l \psi(0) + |\Delta\bar{Q}_{g,max}^*| \sum_{t=0}^{l-1} \epsilon_{max}^{l-t-1} + \\ &\quad C_1 C_3 v_{g,max} e^{-C_2} \sum_{t=0}^{l-1} \epsilon_{max}^{l-t-1} \underbrace{\|i_g(tm) - i_g^*(tm)\|}_{\mathcal{T}_3} \end{aligned} \quad (29)$$

where, $\epsilon_{max} = \max_k |\epsilon(k)| < 1$ represents the contractivity rate and $|\Delta\bar{Q}_{g,max}^*| = \max_k |\Delta\bar{Q}_g^*(k)|$ is the maximum change in the optimal solution to (17) between two OFO sampling times. We now focus on the term \mathcal{T}_3 which is concerned with the transients in the inner loop:

$$\begin{aligned}
T_3 &\stackrel{(a)}{\leq} \|i_g(tm) - i_g^*((t-1)m)\| + \|i_g^*((t-1)m) - i_g^*(tm)\| \\
&\stackrel{(b)}{\leq} C_1 e^{-C_2 m} \|i_g((t-1)m) - i_g^*((t-1)m)\| + 2i_{g,max} \\
&\stackrel{(c)}{\leq} \left(C_1 e^{-C_2 m} \right)^t \|i_g(0) - i_g^*(0)\| + 2i_{g,max} \left(\frac{1 - (C_1 e^{-C_2})^t}{1 - C_1 e^{-C_2}} \right). \tag{30}
\end{aligned}$$

In (a), we add and subtract $i_g^*((t-1)m)$ and use triangle inequality on the norm. In (b), we use the exponential stability property in Assumption 2, tracing till the previous OFO sampling time. Further, the current constraint in (17c) ensures that $\|i_g^*(k) - i_g^*(m)\| \leq i_{g,max}, \forall k, m$. In (c), we trace the recursive relation in (b) to its initial conditions. In (30), we note that sufficient time-scale separation between the OFO and the inner control loop is required for convergence, i.e. T_s must be sufficiently high so that $C_1 e^{-C_2 m} = C_1 e^{-C_2 T_s / T_c} < 1$. By inserting (30) in (29) and using properties of geometric series at the limit of $l \rightarrow \infty$, we obtain the final asymptotic result in (21).

REFERENCES

- [1] J. Rodríguez, S. Bernet, B. Wu, J. O. Pontt, and S. Kouro, "Multilevel voltage-source-converter topologies for industrial medium-voltage drives," *IEEE Transactions on Industrial Electronics*, vol. 54, no. 6, pp. 2930–2945, 2007.
- [2] J. Rodríguez, C. García, A. Mora, S. A. Davari, J. Rodas, D. F. Valencia, M. Elmorsheyd, F. Wang, K. Zuo, L. Tarisciotti, F. Flores-Bahamonde, W. Xu, Z. Zhang, Y. Zhang, M. Norambuena, A. Emadi, T. Geyer, R. Kennel, T. Dragicevic, D. A. Khaburi, Z. Zhang, M. Abdellahem, and N. Mijatovic, "Latest advances of model predictive control in electrical drives—part ii: Applications and benchmarking with classical control methods," *IEEE Transactions on Power Electronics*, vol. 37, no. 5, pp. 5047–5061, 2022.
- [3] N. R. Zargari, Z. Cheng, and R. Paes, "A guide to matching medium-voltage drive topology to petrochemical applications," *IEEE Transactions on Industry Applications*, vol. 54, no. 2, pp. 1912–1920, 2017.
- [4] R. Teodorescu, M. Liserre, and P. Rodríguez, "Grid converters for photovoltaic and wind power systems," *Wiley-IEEE Press*, 2007.
- [5] B. Shakerighadi, N. Johansson, R. Eriksson, P. Mitra, A. Bolzoni, A. Clark, and H.-P. Nee, "An overview of stability challenges for power-electronic-dominated power systems: The grid-forming approach," *IET Generation, Transmission & Distribution*, vol. 17, no. 2, pp. 284–306, 2023.
- [6] Siemens, "Drives for every demand the sinamics family of medium voltage drives," Nuremberg, Germany, 2019, article No.: PDLD-Y10038-01-7600. Dispo 41505 TH 455-190527.
- [7] O. Gomis-Bellmunt, S. D. Tavakoli, V. A. Lacerda, and E. Prieto-Araujo, "Grid-forming loads: Can the loads be in charge of forming the grid in modern power systems?" *IEEE Transactions on Smart Grid*, vol. 14, no. 2, pp. 1042–1055, 2022.
- [8] M. Schneeberger, F. Dörfler, and S. Mastellone, "Sos construction of compatible control lyapunov and barrier functions," *IFAC-PapersOnLine*, vol. 56, no. 2, pp. 10428–10434, 2023.
- [9] H. Abu-Rub, J. Holtz, J. Rodriguez, and G. Baoming, "Medium-voltage multilevel converters—state of the art, challenges, and requirements in industrial applications," *IEEE Transactions on Industrial Electronics*, vol. 57, no. 8, pp. 2581–2596, 2010.
- [10] N. Baeckeland, D. Chatterjee, M. Lu, B. Johnson, and G.-S. Seo, "Overcurrent limiting in grid-forming inverters: A comprehensive review and discussion," *IEEE Transactions on Power Electronics*, vol. 39, no. 11, pp. 14 493–14 517, 2024.
- [11] M. A. Desai, X. He, L. Huang, and F. Dörfler, "Saturation-informed current-limiting control for grid-forming converters," *Electric Power Systems Research*, vol. 234, p. 110746, 2024.
- [12] B. Fan and X. Wang, "Impact of circular current limiters on transient stability of grid-forming converters," in *2022 International Power Electronics Conference (IPEC-Himeji 2022- ECCE Asia)*, 2022, pp. 429–434.
- [13] A. H. Abolmasoumi and B. Marinescu, "State anti-windup: A new methodology for tackling state constraints at both synthesis and implementation levels," *arXiv preprint arXiv:2406.13374*, 2024.
- [14] J. Chen, C. Ge, D. Qiang, H. Geng, T. O'Donnell, and F. Milano, "Impact of frequency anti-windup limiter on synchronization stability of grid feeding converter," *CSEE Journal of Power and Energy Systems*, vol. 9, no. 5, pp. 1676–1687, 2023.
- [15] R. Bernal and F. Milano, "A complex frequency-based control for inverter-based resources," *arXiv preprint arXiv:2501.00448*, 2024.
- [16] M. A. A. Murad, M. Liu, and F. Milano, "Modeling and simulation of variable limits on conditional anti-windup pi controllers for vsc-based devices," *IEEE Transactions on Circuits and Systems I: Regular Papers*, vol. 68, no. 7, pp. 3079–3088, 2021.
- [17] M. Picallo, L. Ortmann, S. Bolognani, and F. Dörfler, "Adaptive real-time grid operation via online feedback optimization with sensitivity estimation," *Electric Power Systems Research*, vol. 212, p. 108405, 2022.
- [18] M. Zagorowska, L. Ortmann, A. Rupenyan, M. Mercangöz, and L. Imsland, "Tuning of online feedback optimization for setpoint tracking in centrifugal compressors," *IFAC-PapersOnLine*, vol. 58, no. 14, pp. 881–886, 2024.
- [19] L. Ortmann, C. Rubin, A. Scozzafava, J. Lehmann, S. Bolognani, and F. Dörfler, "Deployment of an online feedback optimization controller for reactive power flow optimization in a distribution grid," in *2023 IEEE PES Innovative Smart Grid Technologies Europe (ISGT EUROPE)*. IEEE, 2023, pp. 1–6.
- [20] C. J. O'Rourke, M. M. Qasim, M. R. Overlin, and J. L. Kirtley, "A geometric interpretation of reference frames and transformations: dq0, clarke, and park," *IEEE Transactions on Energy Conversion*, vol. 34, no. 4, pp. 2070–2083, 2019.
- [21] T. Geyer, G. Papafotiou, and M. Morari, "Model predictive direct torque control—part i: Concept, algorithm, and analysis," *IEEE transactions on industrial electronics*, vol. 56, no. 6, pp. 1894–1905, 2008.
- [22] P. Tiitinen and M. Suranra, "The next generation motor control method, dtc direct torque control," in *Proceedings of International Conference on Power Electronics, Drives and Energy Systems for Industrial Growth*, vol. 1. IEEE, 1996, pp. 37–43.
- [23] T. Geyer, *Model predictive control of high power converters and industrial drives*. John Wiley & Sons, 2016.
- [24] B. Fan and X. Wang, "Fault recovery analysis of grid-forming inverters with priority-based current limiters," *IEEE Transactions on Power Systems*, vol. 38, no. 6, pp. 5102–5112, 2023.
- [25] A. Hauswirth, Z. He, S. Bolognani, G. Hug, and F. Dörfler, "Optimization algorithms as robust feedback controllers," *Annual Reviews in Control*, vol. 57, p. 100941, 2024.
- [26] S. Chandrasekaran, G. D. Pasquale, G. Belgioioso, and F. Dörfler, "Network-aware recommender system via online feedback optimization," *arXiv preprint arXiv:2408.16899*, 2024.